Millersville University of Pennsylvania

Partial Eclipse Effects on WRF-YSU Single Column Model Planetary Boundary Layer Structures in Relation to Turner et al., 2018

A Senior Thesis Submitted to the Department of Science and Technology & The University Honors College In Partial Fulfillment of the Requirements For the University Honors College & Departmental Honors Baccalaureate

By: Wesley C. Taylor

October 30th, 2024

Acknowledgments:

This thesis would not have been possible to complete without the unflagging support of Dr. Blumberg, Dr. Casas, and Dr. Ward in spite of the many challenges that encompassed this journey. More specifically, I would like to thank Dr. Blumberg for his technical expertise on subject matter that allowed us to catch multiple errors both before and after they had surfaced, Dr. Casas for her advice when it came to assessing what should and should not be left on the cutting room floor and help with pinpointing how to restitch the essay so that it would have a better structure, and Dr. Ward for providing insight on experimental design and validating the logic behind conclusions reached herein.

There are a multitude of others who helped to contribute to the completion of the thesis, faculty and otherwise, who I would also like to thank. Thank you Dr. Sikora for your patience with the thesis completion, Mr. David “Dave” Fitzgerald, Matthew Teare, and Peter Freedman for their combined assistance with troubleshooting technical difficulties, Dr. Yalda and Dr. DeCaria for being bedrocks of support, Dr. Wolfgang for his assistance with thesis completion processes, Dr. Marquez for her assistance with navigating paperwork, my parents and sister for their support even as completion of the thesis dragged on, and last but not least Dr. Clark for his words of encouragement and helping to ignite my passion for research.

Committee Signature Page:

This thesis was completed in the Department of Earth Sciences,

Defended before and approved by the following members of the Committee:

_____

Dr. Greg Blumberg, Ph.D. (Thesis Advisor)

Assistant Professor of Meteorology

_____

Dr. Eleanor Casas, Ph.D.

Assistant Professor of Meteorology

_____

Dr. Chuck Ward, Ph.D.

Professor of Philosophy

Abstract:

The August 21, 2017, total solar eclipse offered a unique opportunity to study planetary boundary layer impacts from a solar eclipse. In Turner et al. 2018, which utilized LiDAR, flux tower, and radiosonde measurements from the Atmospheric Radiation Measurement Southern Great Plains (ARM-SGP) site. Significant effects of the eclipse were observed on the planetary boundary layer (PBL) not only at the surface but also aloft in a region of roughly 89% eclipse coverage across three coordinated sites. Taking radiosonde data from Lamont, OK at 2329 UTC 8/20/2017 as the initial conditions, runs of the Weather Research and Forecasting single column model were conducted using the Yonsei University PBL parameterization scheme. These runs were conducted with and without eclipse Besselian elements being applied to the model shortwave radiation physics to study PBL evolution. Our simulations reproduce some of the Turner et al. 2018 observations, particularly the collapse in the PBL depth reminiscent of the evening transition and the development of an eclipse-generated low level jet approximately 300 meters above the surface. The simulation appears to indicate that single column models can reproduce PBL evolution even in the rare case of a solar eclipse.

Table of Contents

1. Introduction

Eclipse dynamics pose unique challenges due to the great number of variables involved across each eclipse, making every eclipse unique. Their relatively low occurrence in comparison to more standard weather phenomena makes studying them difficult, but their predictability allows for preparation well ahead of future events, which is why Lamont, OK will be of particular interest for this paper. Solar eclipses occur when the moon is positioned between the Sun and Earth in such a way that it casts a shadow over parts of the Earth. In a total solar eclipse, the moon fully covers the Sun relative to an observer on Earth within a narrow region known as the path of totality, and beyond this narrow region where there remains coverage exists a partial solar eclipse, the effects of which will be scrutinized herein. Eclipse modeling exists as a largely underdeveloped field, with even less exploration into single column model (SCM) simulations due to the desire for experimental accuracy and data verification. Attempting to understand how these phenomena operate on the small scales simulated by SCMs will allow for improved understanding of how large-scale influences on the atmosphere affect localized regions, which can then be reapplied to case studies and our general understanding of weather processes.

1.a **Overview of Planetary Boundary Layer Concepts**

The planetary boundary layer (PBL) is a diurnal cycle driven by incoming solar radiation (insolation). This process is extensively covered in Stull (1988). A conceptual model was developed to describe this process, which can be seen in Fig 1. At sunrise, insolation begins to heat the surface, driving the formation of the entrainment zone through convection. As surface heating continues, the height of the entrainment zone begins to rapidly increase until the convection can no longer support entrainment zone growth. Beneath the entrainment zone exists the mixed layer, where vertical turbulence driven by surface heating continuously mixes the atmosphere. At sunset, when insolation is cut off, surface heating ceases and the mixed layer collapses. The entrainment zone, still aloft, retains some of its turbulent motion, forming the residual layer. Meanwhile, as the surface cools, a temperature inversion forms as the air above it has not yet cooled to match the surface, creating the stable layer (Stull, 1988).

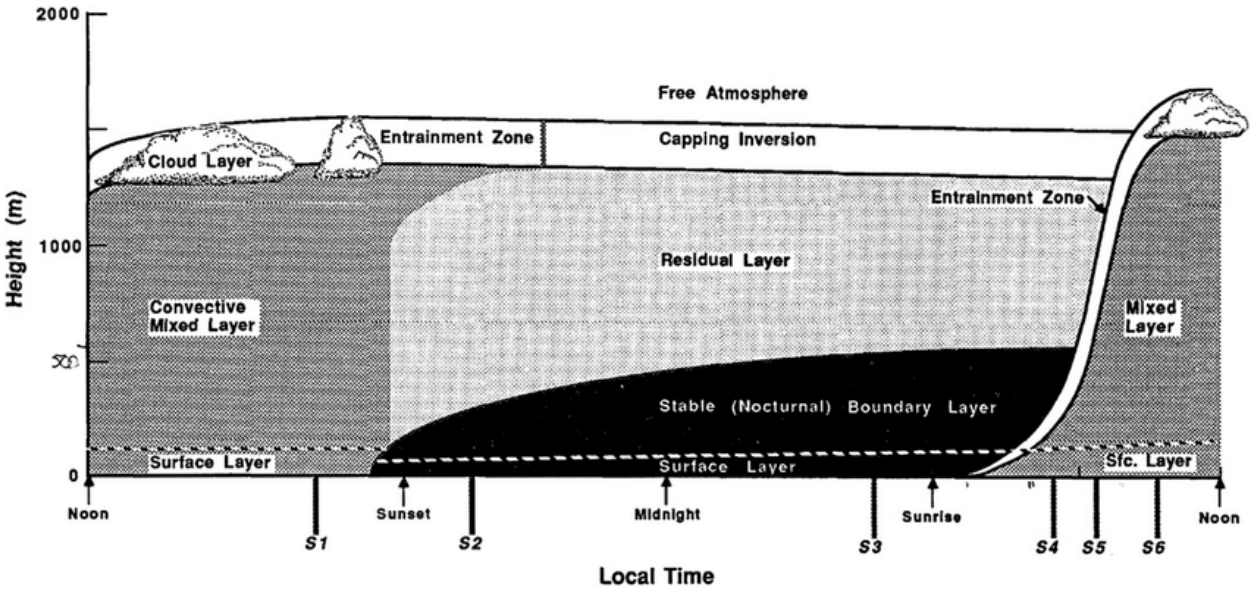

Figure 1: Diurnal PBL visual aid from Stull (1988).

1.b **Low Level Jet Background**

The PBL process can generate what is known as a Nocturnal Low Level Jet (NLLJ), which is defined as a temporary uptick in aloft wind speed well after the sun sets. These processes can be described through a combination of Blackadar (1957), Markowski (2011), and Moene et al. (2010), as will be elaborated herein. During the daytime hours, a balance is struck between Coriolis force, pressure gradient acceleration, and the surface frictional force that is being vertically distributed across the PBL by convection. When convection ends, the upper and middle portions of the PBL exhibit a closer balance in friction to that of the free atmosphere above. This relaxation in vertically distributed friction allows wind to accelerate in those regions, now unbound from their former restraint. This wind will eventually oscillate back towards its calmer state given enough time but is typically prevented from doing so with the commencement of the next day's convection. Additionally, the strength of this frictional force also affects the strength of the NLLJ – the stronger the convective friction, the stronger the following NLLJ response.

There exist a number of factors that have the potential to influence NLLJ formation and strength. Among the greatest of these modulators is that of the Coriolis force. As the initial dominance of the pressure gradient force wanes after friction ceases, the Coriolis force bends the winds in its direction to match the rotational direction of the Earth. This can result in a wind maximum as existing wind patterns and Coriolis-augmented motion align, allowing for the enhancement of existing winds, especially in relation to NLLJs (Blackadar, 1957). Large regions of sloping terrain, as can be found in the Great Plains, are known to enhance NLLJs due to a reversal of thermal wind resulting from the development of stable stratification that suppresses east-west motion (Holton, 1967).

Though the exact greatest magnitude of an NLLJ is somewhat difficult to predict, much less generalize, the time of greatest magnitude can be calculated. The period of time it takes for an oscillation to complete is dependent on latitude and is shorter in regions farther from the equator. Since the NLLJ maximum typically occurs when the wind becomes supergeostrophic, or about 5/12ths of the way through this oscillation, so long as the oscillation period is known, so too is the approximate time for the onset of the strongest point of the NLLJ. If convection begins to falter at around 6-7pm local time, and since this period takes roughly 20 hours at the latitude of Lamont, OK (36.605 N), the NLLJ should be expected to crest roughly 8.4 hours after the initial disruption, or between 2:30 and 3:30 am local time.

1.c **Prior Study of Eclipses on the Planetary Boundary Layer**

One such study that examined the effects of solar eclipses on the PBL is Turner et al. (2018; hereafter referred to as T18). The location of the study sites used, as seen in Fig. 2, were in regions of roughly 89% coverage. A total solar eclipse would therefore be expected to have similar effects with a greater magnitude.

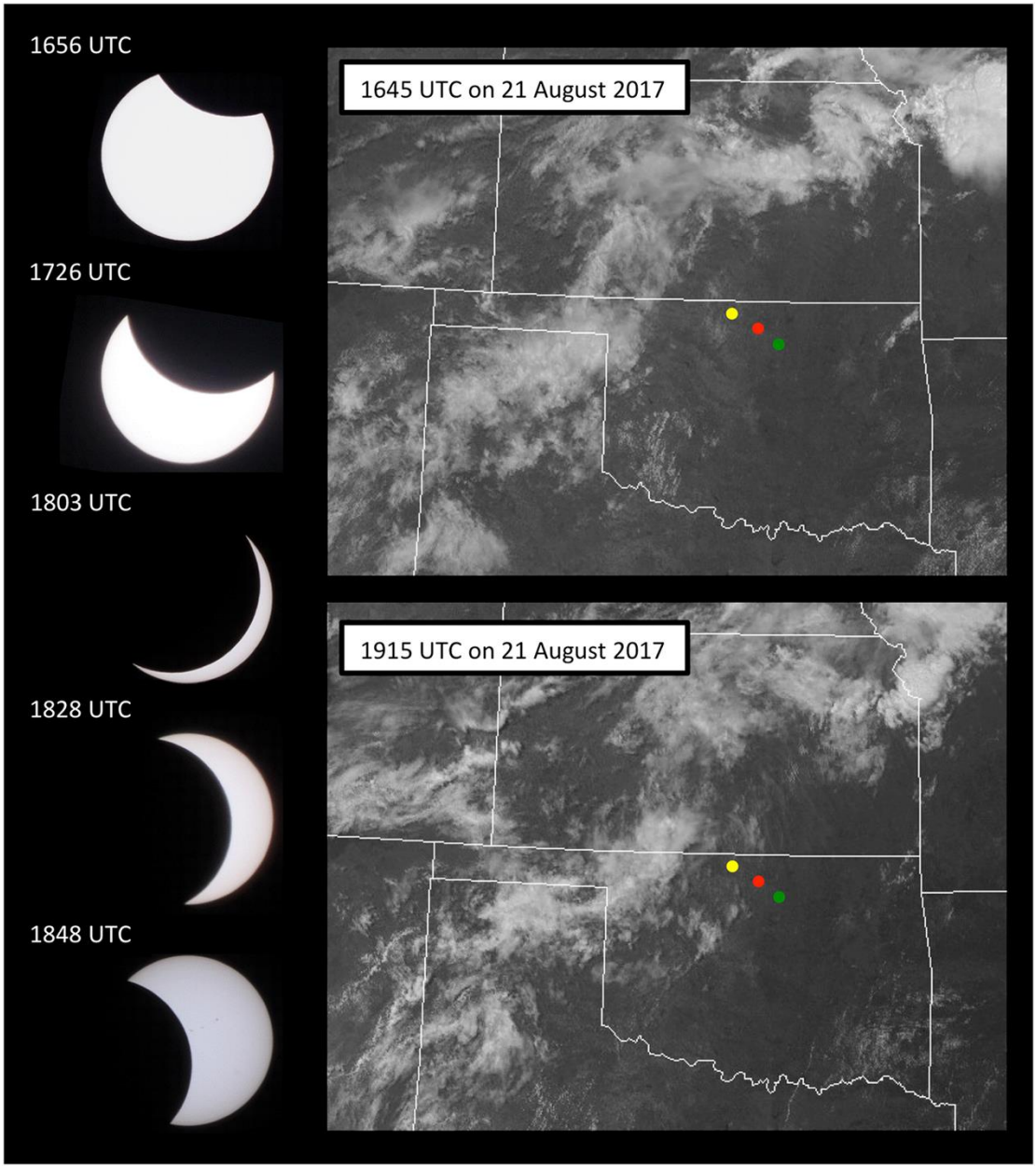

Figure 2: "Figure 1" as reproduced from Turner et al. (2018). "(left) Photos of the solar eclipse taken at the C1 site and (right) visible geostationary satellite images taken before and after the eclipse. The yellow, red, and green dots indicate the locations of the E32, C1, and E39 sites, respectively (the satellite images were downloaded from the National Center for Atmospheric Research MMM image archive at **http://www2.mmm.ucar.edu/imagearchive/**)."

A suite of instruments were utilized at all three sites as found in Fig. 2 to gather data on near-surface eclipse effects. A list of these instruments, as well as general site information, can be

found in Table 1. Of the three sites, the Lamont, OK/C1 site has the greatest number of instruments and is therefore of overall greatest interest.

Table 1: Table 1 as reproduced from Turner et al. (2018), "Information About Each of the Sites Used in the Paper"

Site Name (Closest Town)	Latitude [^{o}N]	Longitude [^{o}E]	Elevation [m MSL]	Minimum DSWF [W m^{-2}]	Mean Sfc Q [g kg^{-1}]	Mean Sfc T [C]	Mean Sfc wind [m s^{-1}]	Instruments	Primary land use
E32 (Medford)	36.819	-97.820	328	56.2	15.7	32.1	5.9	AERI, DLID, SfcMet, EBBR, solar radiometers	Pasture
C1 (Lamont)	36.605	-97.485	318	84.2	14.5	31.5	7.3	AERI, DLIDx2, SfcMet,ECOR,RLID, solar radiometers	Pasture, wheat stubble
E39 (Morrison)	36.374	-97.069	279	86.9	16.2	31.2	6.1	AERI, DLID, SfcMet, ECOR, solar radiometers	Pasture and soybeans

"Note. The closest towns to each site, all of which are in Oklahoma, are within 15 km. These sites are shown in Figure 1 as yellow (E32), red (C1), and green (E39) dots. DSWF: downwelling shortwave flux (at the surface), Sfc: surface (i.e., 2 m AGL), Q: water vapor mixing ratio, T: ambient temperature, AERI: Atmospheric Emitted Radiance Interferometer, DLID: Doppler lidar, SfcMet: surface meteorological station, EBBR: energy balance Bowen ratio station, ECOR: eddy correlation station, RLID: Raman lidar. The land use column captures the primary land use in the area surrounding each site." (T18)

The data gathered from all three sites would be used to make general assessments about meteorological conditions, which were split between surface heat fluxes, general parameters in reference to their means, vertical motion and vertical velocity variance, and potential temperature in Figure 4, and Doppler LiDAR horizontal wind speed and moisture assessments as seen in Figure 5. In brief, the near-surface vertical wind speed and gust occurrence decreased at the time of and for some time after the eclipse, with aloft vertical velocity variance collapsing at about 1 km AGL, with a general decrease at all levels before returning to a neutral-to-positive state over about 30 mins, ascending from the surface. Potential temperature was found to decrease at the surface, acquiring maximum strength and depth between 15-25 minutes after the point of maximum obscuration. Furthermore, winds were found to be backing as the event progressed. Turbulent kinetic energy was found to substantially decrease in a pattern similar to that observed in the vertical velocity variance profile. The water vapor mixing ratio was found to decrease within the lowest 400m of the atmosphere 30 minutes prior to the onset of the eclipse and would

not rebound until 90 minutes after the eclipse. Shared with the regions of decreased vertical velocity variance and turbulent kinetic energy is a region of increased horizontal wind speed, which would itself dissolve as vertical mixing resumed from the surface.

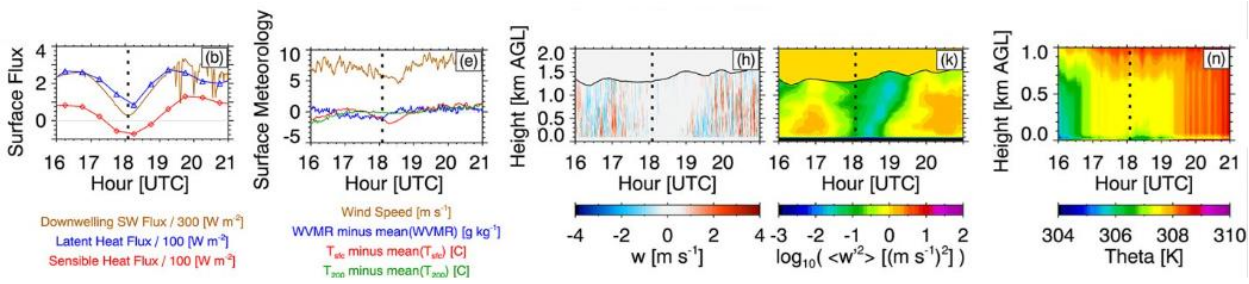

Figure 4: Figure 2 as adapted from T18. Description edited for clarity, but otherwise from T18. "Observations at the SGP site on 21 August 2017 from 16:00 to 21:00 UTC. Downwelling shortwave (brown), sensible heat (red), and latent heat (blue) fluxes at the surface (b); 10 m wind speed (brown) and deviations of the 2 m temperature (red), 2 m water vapor mixing ratio (blue), and 200 m temperature (green) from the mean (e) where the mean values are given in Table **1**; profiles of vertical motions at 1 s resolution (h); profiles of the variance (30 min resolution but calculated every 10 min) of the vertical motions (k); and potential temperature profiles at 5 min resolution (n). This row corresponds to observations at the C1 site. The dashed vertical lines in all panels indicate the time of maximum solar eclipse. The solid black line in (h) denotes the level where the lidar's signal-to-noise ratio drops below −21 dB; points above that level are very noisy and not shown. Note that (n) has a different vertical range (0 to 1 km) relative to the other time-height cross sections in (h) (0 to 2 km)."

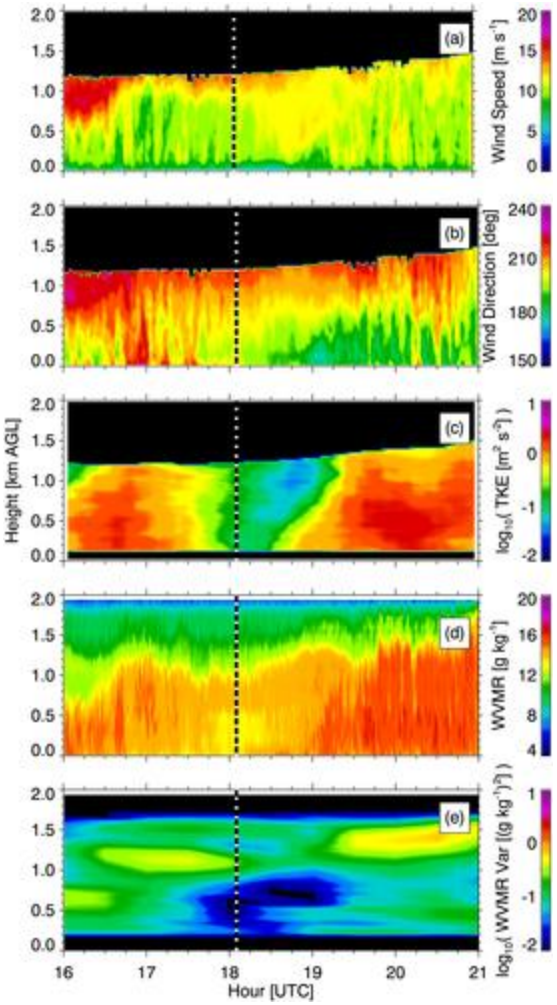

Figure 4: Figure 3 as reproduced from T18. “Profile observations at the Southern Great Plains C1 site on 21 August 2017 from 16:00 to 21:00 UTC. (a) Horizontal wind speed (1 min resolution), (b) horizontal wind direction (1 min resolution), (c) turbulent kinetic energy (15 min resolution), (d) water vapor mixing ratio (10 s resolution), and (e) water vapor mixing ratio variance (30 min resolution). The times correspond to the middle of the averaging periods.”

In what is described as a rapid ‘afternoon-sunset-sunrise-afternoon' pattern, the boundary layer collapses due to the sudden lack of insolation, leading to the temporary formation of a stable layer and Eclipse Low Level Jet (ELLJ) before the mixed layer reforms. A conceptual model for this phenomenon can be seen in Fig 5. The ELLJ is expected to form aloft after the onset of mixed layer collapse at approximately 1km AGL, which then expands both upwards but mostly downwards. ELLJs are short-lived by nature, existing only until the mixed layer rebuilds itself as insolation drives time-lagged convection after the eclipse has begun to pass. ELLJ maximum height AGL is believed to decrease with time after reaching its absolute maximum height, though the natural conclusion of where they end is cut short by the reintroduction of the mixed layer. ELLJ effects would therefore only be minimally noticeable at the surface, with the majority of its effects manifesting aloft.

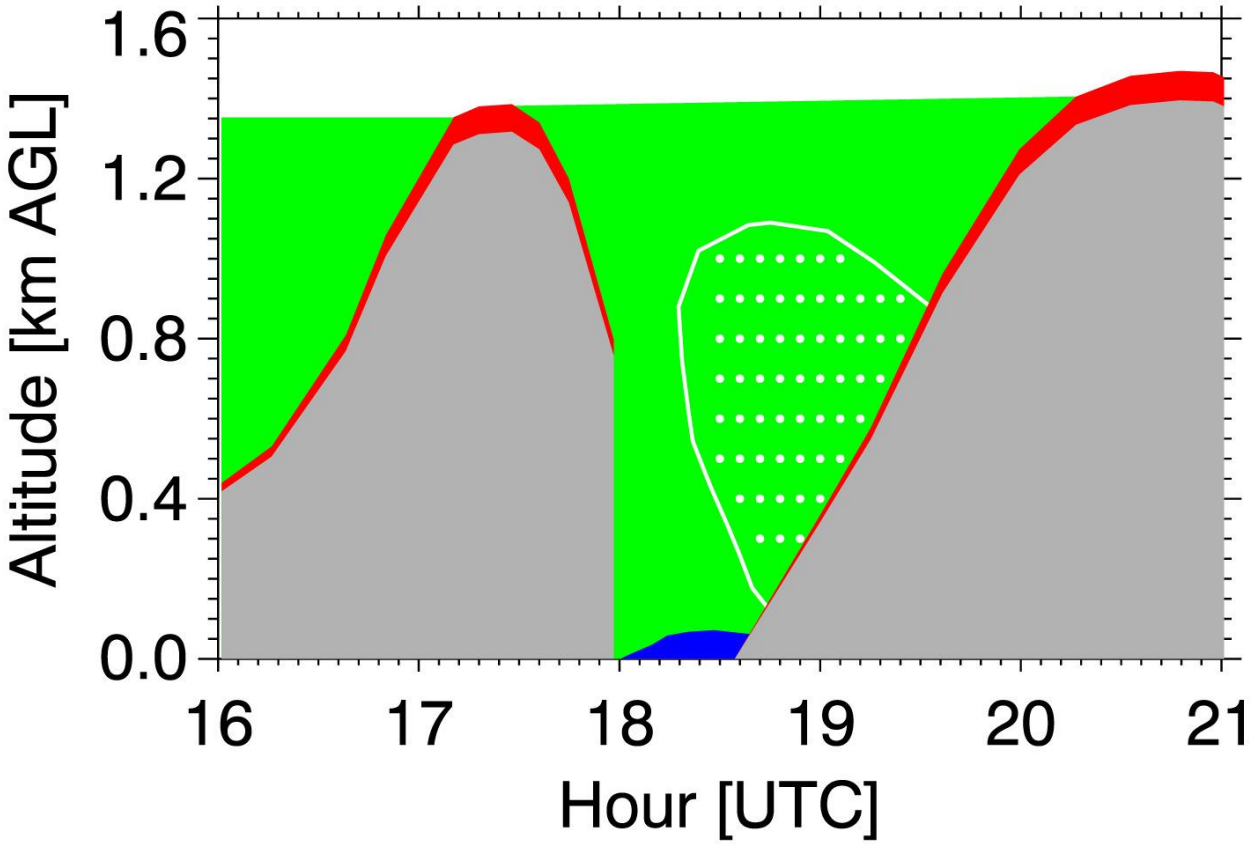

Figure 5: Figure 4 as reproduced from T18. "A conceptual diagram from T18 depicting the evolution of the convective boundary layer (gray), residual layer (green), interfacial layer (red), stable boundary layer (blue), and low-level jet (white bounded dotted region) during the eclipse event."

2. **Study Goals**

This paper focuses on the total solar eclipse that occurred on August 21st, 2017. Beginning in Oregon at 10:16 am local time and traveling across the United States through to South Carolina at 2:48 pm local time, the greatest length of totality for any location lasted for 2 minutes 40 seconds. Most of the United States still experienced at least a partial solar eclipse, with regions closer to totality receiving greater effects than regions further away, which is why T18 was performed in the region that it was.

Figure 6: Map of the 2017 total solar eclipse event. Credit: NASA

The T18 study utilized a suite of instruments across multiple sites to analyze eclipse effects on PBL parameters while remaining outside of the path of totality. As the exact mechanisms behind ELLJ formation remain largely obscured, simulating the conditions leading into, of, and after the 2017 eclipse as exhibited in T18 will allow for analysis of the potential for ELLJ formation using SCM. Specifically: 1) Are eclipse effects on the surface an exclusively local phenomenon and would therefore be able to be replicated by SCM; 2) Are the effects too large-scale such that small-scale simulations are inadequate in capturing any effects, particularly that of ELLJ development; and 3) How well does the model reproduce the effects of the eclipse, if it is able to, in relation to T18?

3 **Experiment Setup**

3.a **Model Setup**

The single-column model (SCM) function of the Weather Research and Forecasting Model (WRF) was used across all simulations produced. Many of the model parameters used were unchanged from the default settings found within the WRF test parameterization scheme or were left at default values. The SCM itself was preprocessed using ideal.exe, having altered certain parameters in the initialization file as well as the start and stop times within force_ideal.nc to allow the simulation to be performed. The WRF Preprocessing System (WPS) was not used during this process as it was unnecessary to do so.

Table 2: Schemes Utilized Within the Simulations

Scheme Type	**Scheme Name**
Model	YSU v3.4.1 (Hong et al., 2006)
Height	Eta Coordinates, Default Stretching
Longwave Radiation	RRTM (AER, inc., 2002)
Shortwave Radiation	Dudhia (1989)
Land Surface Model	Unified Noah-MP
Surface Layer	Revised MM5 Monin-Obhukhov (Jimenez et al., 2012)
Microphysics	Lin et al. (1983)
Cumulus Physics	N/A (Disabled)
Eclipse Besselian Elements	Torrecillas et al. (2015)
Time Integration	Runge-Kutta 3rd Order
Hydrostatic	N/A (Non-hydrostatic)
Horizontal Advection	N/A (Disabled)

The SCM utilized a 3x3 grid comprised of five 4km x 4km squares. The square from which all information was gathered was the center grid point, with the remaining four adjacent squares in the immediate north, south, east, and west utilized to set boundary conditions. Due to processing limitations, the model was run in serial on the JetStream2 supercomputer service through UCAR. The height ceiling was established at 100 mb.

The shortwave eclipse scheme was set to active for the eclipse simulation as established by Torrecillas et al. (2015), with the corresponding Besselian elements supplied to the WRF for calculations. This scheme alters shortwave calculations according to Sun-Moon-Earth geometry based on their known orbital periods, solar angle, angle of the Moon's shadow relative to an observer's position on Earth, Earth's rotational period, and small changes in Earth's rotational period with time to generate the effects of an eclipse in the simulation.

The YSU v3.4.1 Hong et al. (2006) model scheme, which is integrated into the WRF, was used across all simulations. The YSU operates on a nonlocal K, centered-in-space approach that explicitly considers top of PBL entrainment. Despite prior criticism of the YSU scheme for its inability to properly predict nighttime PBL conditions – especially NLLJs - the 3.4.1 version has shown to improve the reliability of NLLJ predictions as discussed in Hu et al. (2013). Given the importance of LLJs to this experiment, high reliability in both PBL and NLLJ predictions is important for gauging the reliability of results.

3.b **Data Used**

Initialization sounding data was pulled from the Integrated Global Radiosonde Archive (IGRA). The sounding launch site was chosen based on relative proximity to the location of the testing sites within T18. The launch site chosen was that of Lamont, OK, located at (36.6N, 97.5W), which has continuous radiosonde data archived dating back to 2000. This site was chosen based on being effectively the same as the central test site within T18 (Fig. 2).[1]

The WRF SCM model requires starting altitude relative to sea level, potential temperature, pressure, geopotential height, wind speed, wind direction in north-south and east-west components, and water vapor mixing ratio within its input soundings. The actual soundings gathered instead contained geopotential height, temperature, a zonal and meridional wind component, and dew point depression. Potential temperature was obtained by using Poisson's equation with the vapor mixing ratio dependent Poisson constant.

[1] The entire simulation may not have taken place in the correct location at all. When doing preliminary research on the topic, it was suggested that the data from which the WRF SCM test data was taken from was the ARM CART site. In attempts to assess the location of viable comparable sites relative to T18, the Lamont, OK site was located in the IGRA database, which revealed that it, too, was an ARM site – but it was actually a site known as ARM SGP, which is situated considerably further south and closer to eclipse totality than ARM CART. This also meant that soil type could no longer be considered 1-to-1, and the soil itself is too cold for the time of year the eclipse occurred, as the soil data from the idealized case was from late October as opposed to late August. Though this does suggest that ELLJs can actually form in harsher conditions than previously assumed by the data's results as described later, having been in a less convective environment and even further from totality than what was exhibited in T18, a) without the data to determine if this hypothetical is the case and b) without the current capability to rerun the relevant simulations to assess the validity of this issue, it is presently impossible to assess the known data in perfect comparison to T18.

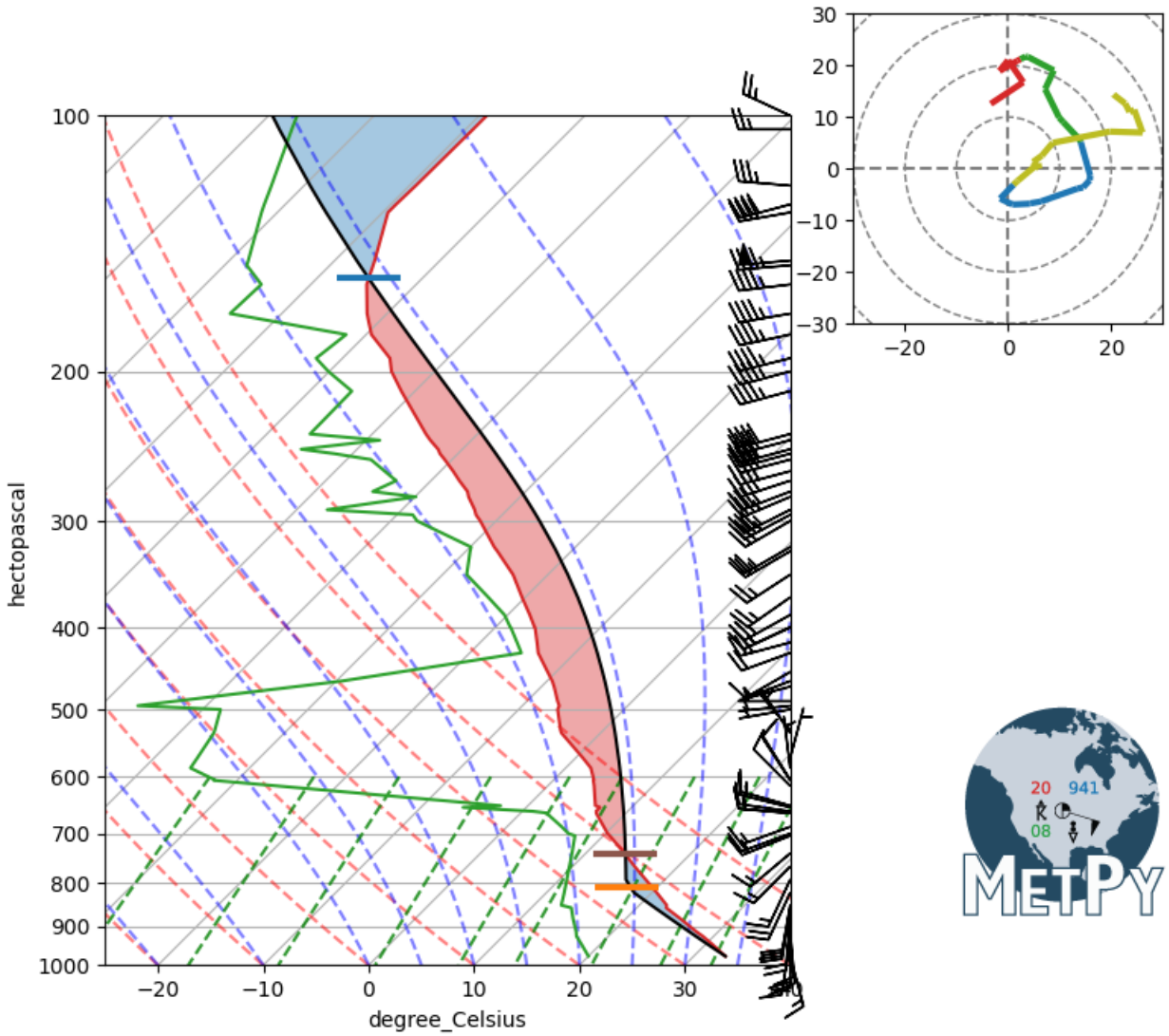

Figure 7: Skew-T utilizing MetPy based on the 8/21 00z sounding launched from the ARM-SGP site at Lamont, OK.

The sounding tested to provide initial conditions for the model occurred at 8/21 00z, which occurred at 8/21 2329 UTC, is represented by Fig. 7. The model was run until 8/22 1129 UTC to allow for full nocturnal boundary layer development and observation of potential eclipse effects. In order to observe whether the eclipse was itself critical to the formation of features that had developed in T18, a pair of simulations was run. The control simulation did not include the Besselian elements to simulate how the day may have progressed in the absence of an eclipse, and the experimental simulation did factor into account the eclipse utilizing Besselian element integration.

4. **Results**

4.a **Heat Budget due to PBL Scheme**

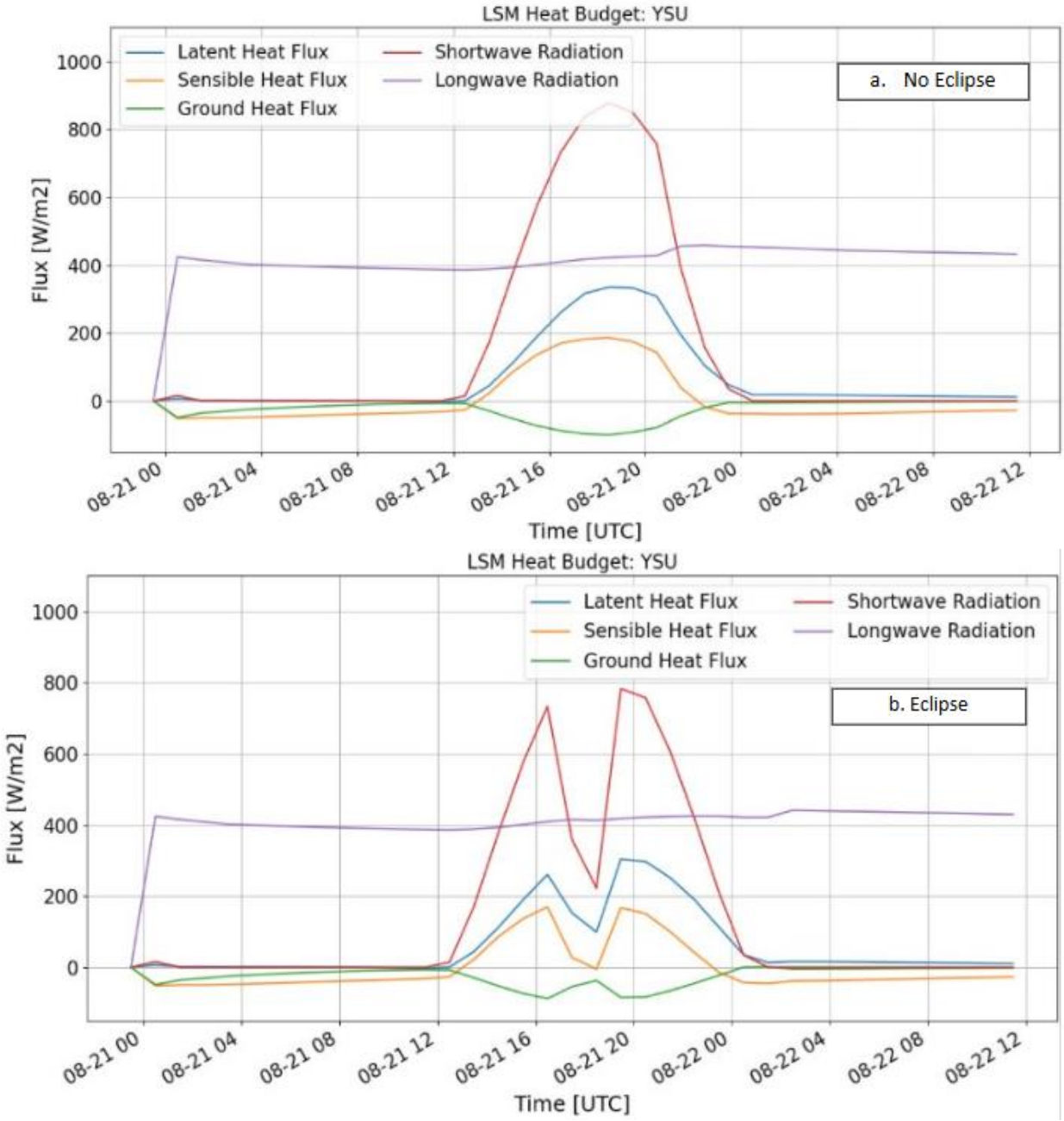

Figures 8a, 8b: Heat Fluxes as simulated by the model. Figure 8.a shows the non-eclipse simulation, Figure 8.b shows the eclipse simulation.[2]

[2] Insolation can be seen to suddenly collapse in Fig. 7a an hour earlier than in Fig. 7b, contaminating all non-eclipse graphs in the section. Since all data was lost during the writing of this paper, there is no way to determine exact

Figure 8 shows the various heat fluxes as they evolve across the day in each the control and experimental model runs. Under normal conditions, incoming shortwave radiation peaks around 875 W/m^2 at solar noon (Fig. 8a). Sensible heat flux peaks about an hour before this maximum, while latent heat flux peaks about an hour after this point. Ground heat flux is positive overnight and negative during the day, with its minimum occurring at about solar noon.

In contrast, insolation values rapidly decrease and increase in response to the movement of the moon in front of the sun in the eclipse simulation (Fig. 8b). The point during which insolation begins to rapidly decrease is at about 16:30 UTC. An apparent inflection point in insolation occurs at approximately 17:30 UTC, which sees insolation begin to decrease less steeply. The minimum insolation that reaches the surface is simulated to occur at 18:30 UTC due to being the time of maximum obscuration, which leads to an immediate increase of insolation that ends at 19:30 UTC at which point insolation has effectively fully rebounded.

The maximum recorded insolation value in the eclipse simulation are about 100 W/m^2 below their eclipseless counterpart. The minimum insolation value for the day occurred at the eclipse's apex, at about 225 W/m^2. Latent and sensible heat flux also exhibit decreases in synchronization with shortwave radiation even as ground heat flux increased. Sensible heat flux dipped below zero as the moon began to cover more of the sun and shortly after the point of greatest obscuration, and approached the same value as ground heat flux at the eclipse's end. Longwave radiation slightly decreases in response to the shortwave decrease, but rebounds quickly once the moon starts moving out from in front of the Sun.

4.b **Potential Temperature due to PBL Scheme**

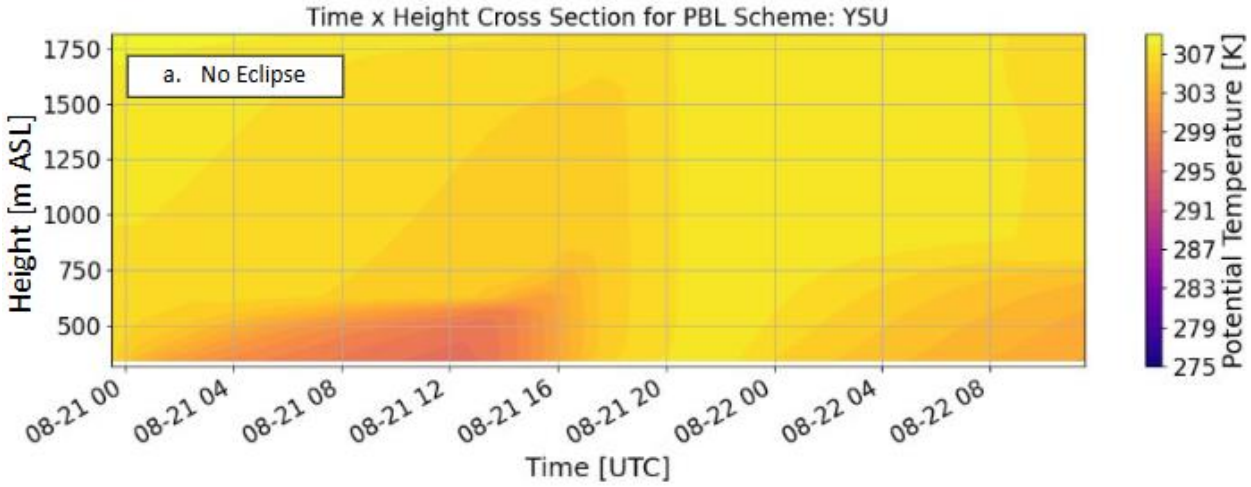

cause, though it may be related to aloft cloud cover from the microphysics scheme. Sunset time is correct in eclipse graphs.

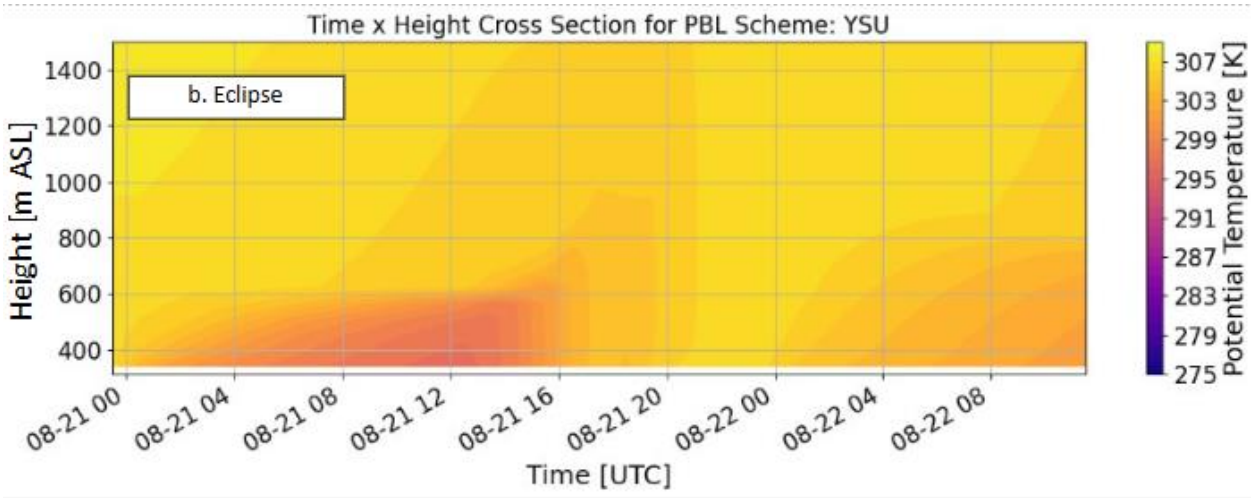

Figures 9a, 9b: Potential Temperature at 1-degree resolution in Kelvin. Figure 9.a shows the non-eclipse simulation, Figure 9.b shows the eclipse simulation. Errata include mismatch of y-axis lengths between 3a and 3b by showing 1500m AGL and 1500m ASL respectively.

As seen in Figure 9a, potential temperature exhibits a deep cool spike through all layers of the boundary layer. Shortly after 20 UTC, potential temperature stabilizes at all depths resultant of thorough mixing. At the onset of nightfall, temperatures begin to decrease at the surface before expanding to a depth of 500m AGL, with potential temperature decreasing at an average rate of 0.5K/hr.

The eclipse simulation deviates from this pattern, with the cooling effects of the eclipse stunting convective warming (Fig. 9b). The lack of insolation generates a short-lived, shallow cool region near the surface, which acts as a de facto stable layer. This stable layer is short-lived, persisting for no more than 15 minutes before dissipating, giving way to more surface heating. This delays proper mixed layer depth development, resulting in a relatively shallower PBL and the depth of the atmosphere being cooler than in the non-eclipse simulation.

4.c **Potential Temperature Rate of Change due to PBL Scheme**

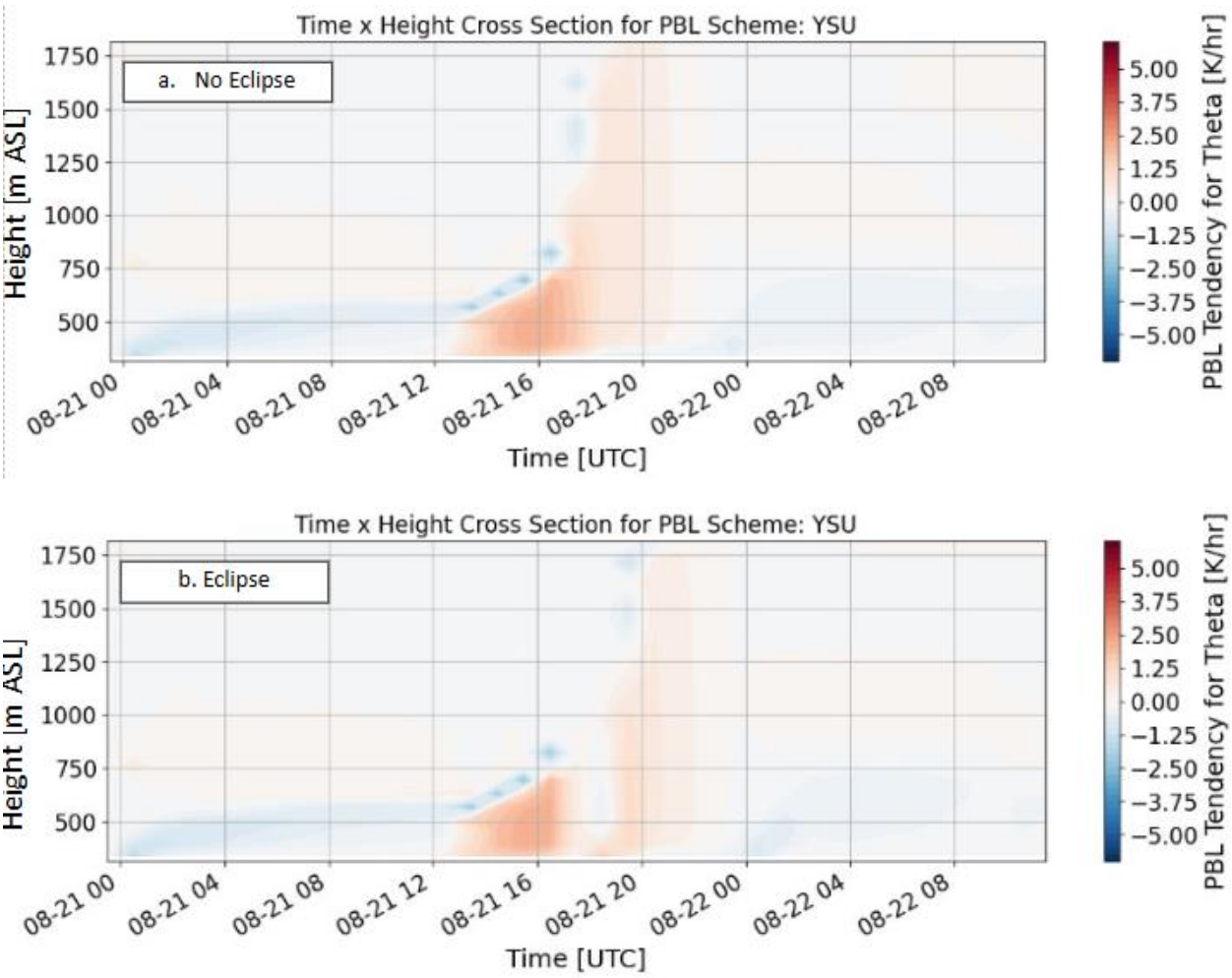

Figures 10.a, 10.b: Temperature tendency through 1500m AGL in terms of Kelvin per hour. Figure 10.a shows the non-eclipse simulation, Figure 10.b shows the eclipse simulation.

The above charts show temperature tendency in K/hr, with red regions showing warming and blue regions showing cooling. During the overnight hours, there exists a persistent cooling region at the surface as the atmosphere stabilizes, with the effect becoming stronger between 50-250m in height. As sunlight begins to warm the surface, the cooling region is forced above the surface heating. This cooling region, despite sharing continuity with the overnight stable layer, now is better used as a tracer for the location of the entrainment zone and therefore also PBL height.

Once the former stable layer has been sufficiently warmed by insolation to a depth of 500m, warming begins to accelerate upwards above the surface layer. As seen in Fig 5a, warming rapidly increases upwards above the surface as the mixing layer matures at around solar noon, beyond which point the PBL fully develops. The magnitude of temperature tendency decreases during the afternoon hours, with the entrainment occurring between it and the free atmosphere as indicated by the aloft cooling regions. Once nightfall occurs, all convective warming ceases, replaced by surface cooling once more. However, there exists a slight warming

region that persists aloft where the PBL had previously reached, indicating the maximum vertical extent of the residual layer and thus the capping inversion.

The simulated eclipse as seen in Fig. 9b has a stark and immediate effect on temperature tendency, with the existing mixed layer and entrainment zone collapsing shortly after its onset. Warming quickly resumes in the lowest few meters near the surface, but between 150m – 400m AGL there exists a short-lived, intense cooling region. The formation of a weak capping inversion in place of the entrainment zone for the duration of the eclipse aloft cooling region is also apparent. Shortly after the greatest extent of the eclipse, heating breaks through this cooling region, reforming the mixed layer to the approximate height of the eclipse-generated capping inversion. It is only after the capping inversion fully warms and returns to its entrainment zone state that PBL height building resumes. The PBL still climbs higher, but never reaches the same height predicted under standard conditions.

4.d **Horizontal Wind Speed due to PBL Scheme**

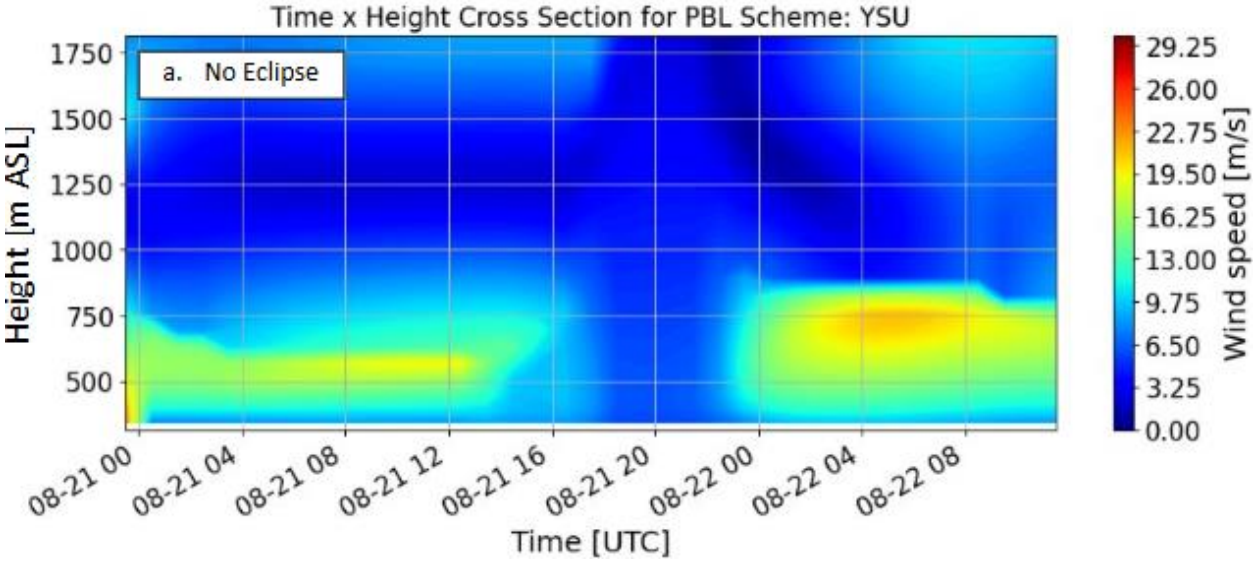

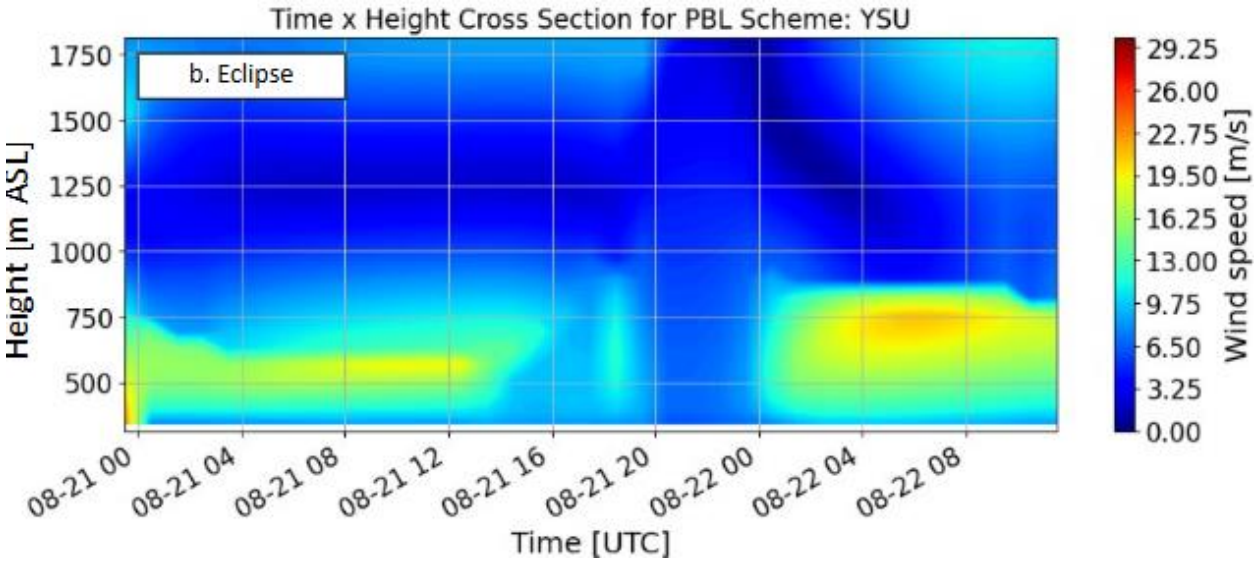

Figures 11a, 11b: Wind speed up to a depth of 1500m AGL in meters per second. Figure 11.a shows the non-eclipse simulation, Figure 11.b shows the eclipse simulation.

As the simulation begins at nightfall, a discussion of horizontal winds should begin with that of the first overnight NLLJ, which is consistent across simulations. Forming aloft within the hours immediately after initialization between 100m and 250m AGL, winds strengthen to roughly 20 m/s. This NLLJ 'core' forms at about 150m AGL and persists until morning convection, with wind speeds increased in strength above said core to about 400m AGL, beyond which point they begin to decrease to a minima near zero at 950m AGL. The NLLJ does not seem to interact much with the surface, as wind speeds rapidly decrease shortly before approaching the surface.

Even as the NLLJ core dissipates, the existing horizontal winds aloft persist until the forming entrainment zone begins to mix those regions of the atmosphere, tempering the winds. It is only after these winds have mixed out that the mixed layer can begin more thorough vertical mixing of the atmosphere that allows it to build towards its maximum height as can be seen in Fig 11.a. The warming near-surface mixed layer below this mixing region has winds decreasing to about 3 m/s until shortly before the mixed layer undergoes rapid height growth, where a column of elevated wind speed of about 9 m/s magnitude persists for no more than 2 hours even as the aloft region is dissipating, beyond which point horizontal winds decrease at all regions below 1km AGL to about 3 m/s in the no eclipse simulation.

Once nightfall occurs, horizontal winds quickly pick up as the previously vertically distributed frictional forces cease. Enhanced by Coriolis forces, a 21 m/s jet core forms at 400m AGL 3 hours after nightfall. This jet core persists for 6-8 hours, peaking in strength between

2:30am and 3:30am, before slowly decreasing in strength and height as the night progresses, presumably decaying after the model ends as a new convective cycle begins with daybreak.[3]

The eclipse model as seen in Fig 11.b begins with the same weak first NLLJ and initial PBL ascent in the early morning hours, but abruptly changes with the onset of the eclipse. Shortly before the onset of T2, winds aloft accelerate from 6 m/s to 12 m/s within 30 minutes. This region extends from the lowest portion of the pre-existing entrainment zone to grazing the surface about an hour after its initial onset shortly after T3 and is the manifestation of an ELLJ.

The ELLJ wind maximum is about 15 m/s at 300m AGL during the same window as when the ELLJ brushes against the surface, showing an enhancement of winds by about 6 m/s over the non-eclipse simulation. As the mixing layer recovers at the surface and conditions cease to be stable, the ELLJ is forced upwards to the approximate height of what was the briefly lived capping inversion. Notably, the shift from entrainment zone to capping inversion, each characterized as such by the thermal change with respect to time as seen in Section 4.c, has little, if any, effect on wind speeds. The reversal of this process also has little effect on wind speed, as the horizontal winds only dissipate as the mixed layer slowly breaks them down.

The PBL never fully recovers from the ELLJ's alterations to the atmospheric environment. Winds that were 'supposed' to have only been about 6 m/s find themselves doubled in the wake of the ELLJ. The aloft winds from the remnants of the previous night's NLLJ, now the entrainment zone, never fully break before nightfall.

4.e **Cross-Comparison Between the Eclipse-Enabled PBL Scheme and Data From the Lamont, OK Site in Turner et al. (2018)**

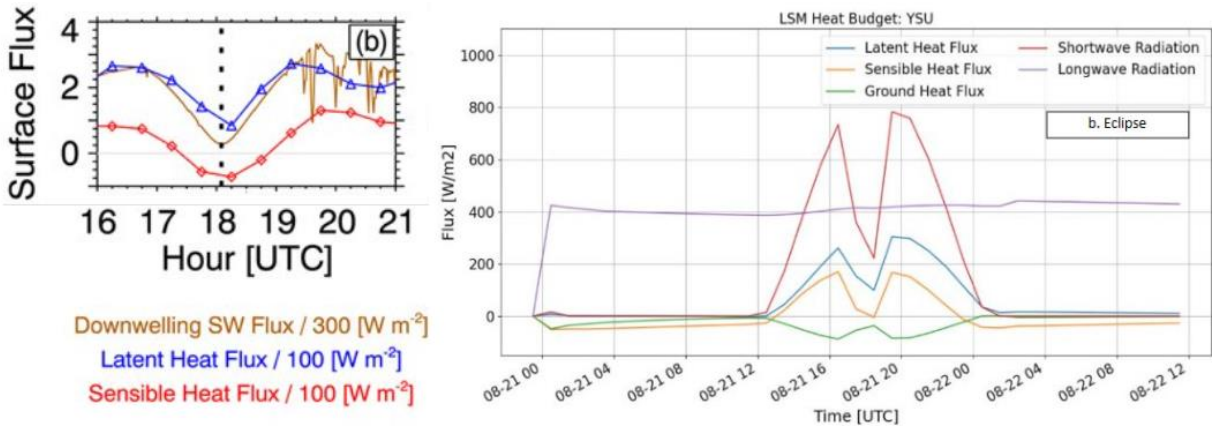

Figure 12: (Left) Panel (b) from Figure 4 as adapted from Figure 2 from T18. (Right) Figure 8.b from Section 4.a.

[3] NLLJ development is altered in 10.a as a result of the early sunset as described in Footnote 2, but the time lag to jet core maximum is still the same amount of time after sunset despite the shift.

The surface-detected flux T18 data is largely similar to that which was simulated, though there do exist some differences, as analyzed in Fig. 12. Latent heat is almost the same at the time of the eclipse, but for all periods unaffected by the eclipse latent heat is higher in reality than in the simulation. Conversely, observed sensible heat is much lower than in the simulation, dropping to nearly –100 W/m^2 at its minimum in comparison to the simulated 0 W/m^2. Recorded incoming shortwave radiation is lower than the simulation both before and after the eclipse but recovers to an overall higher value after the eclipse's resolution when not taking clouds into account. Additionally, the minimum insolation value recorded in T18 is about one third of that which was simulated, meaning that effects driven by insolation collapse should be stronger than what was recorded by the model.

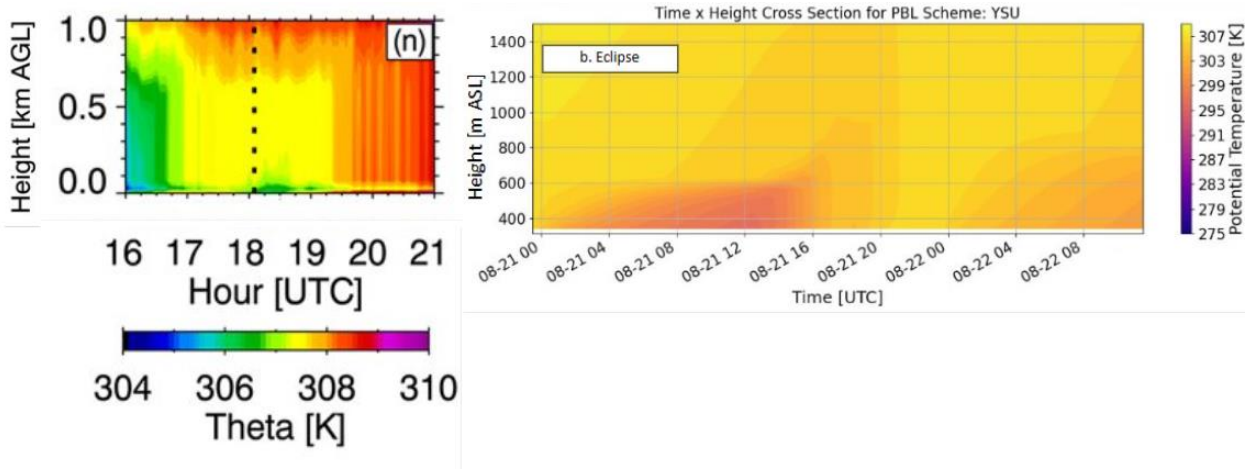

Figure 13: (Left) Panel (n) from Figure 4 as adapted from Figure 2 from T18. (Right) Figure 9.b from Section 4.b.

When looking at the eclipse event from the perspective of atmospheric potential temperature as can be seen in Fig. 13, the depth and duration of the eclipse's effects on the surface are roughly matched by the simulation, though the depth of the cooled region is slightly higher in the observations than in the simulation. However, the potential temperature across the full depth of the atmosphere is higher in reality than in the simulations, with the region above the eclipse-cooled region being 3-4K warmer than that observed by the simulations.

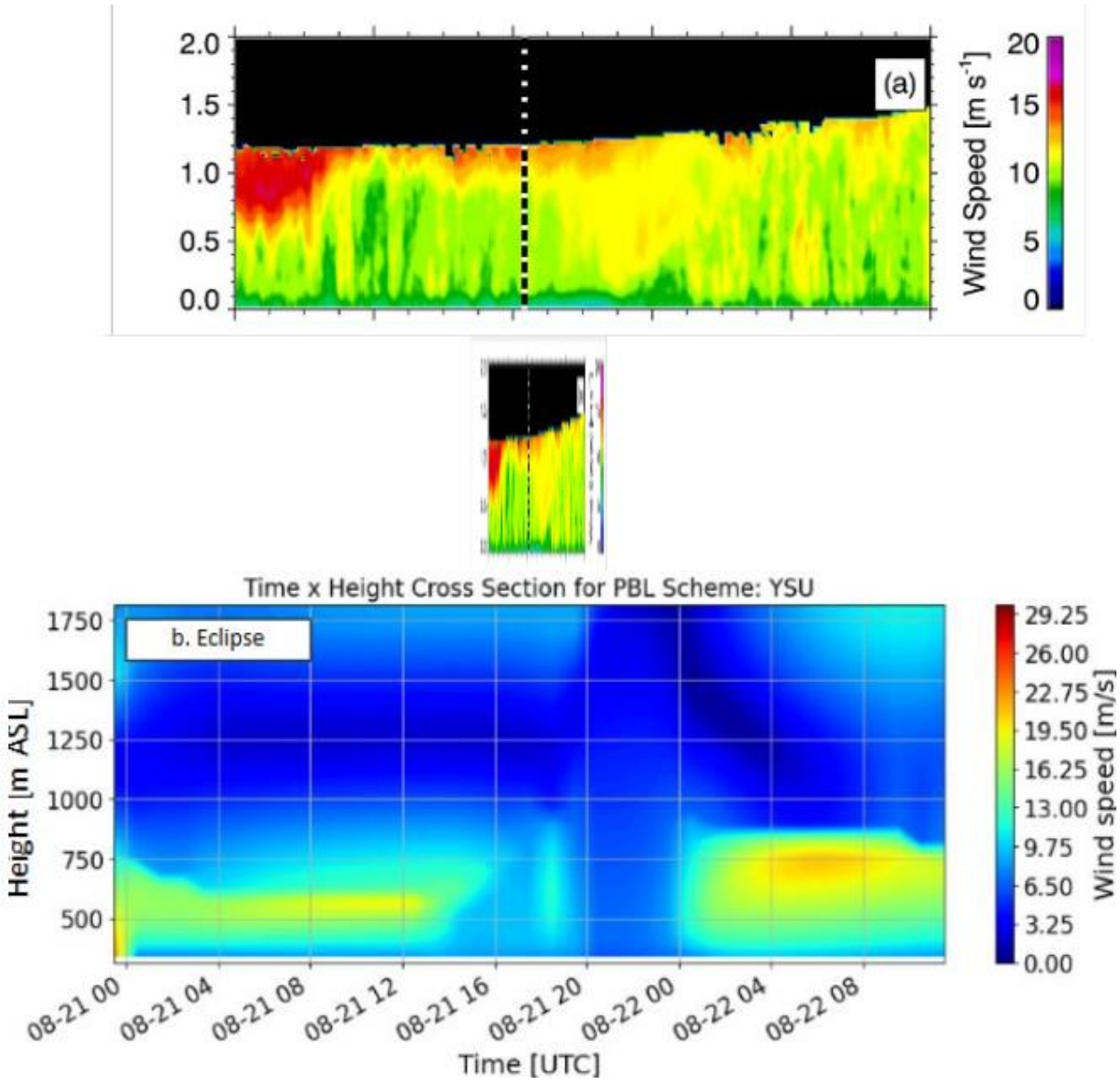

Figure 14: (Top) Panel (a) from Figure 4 as adapted from Figure 3 from T18 at standard resolution. (Middle) Panel (a) from Figure 4 as adapted from Figure 3 from T18, horizontally scaled to match the time scale from Figure 11.b from Section 4.d. (Bottom) Figure 11.b from Section 4.d. All figures are horizontally aligned so that the time of eclipse occurs at the same point in all graphs simultaneously for visual clarity.

The horizontal wind speed graphs, when comparing them as in Fig. 14, both verify the existence of an ELLJ, with the magnitude of being roughly the same across each T18 and the simulation. However, the depth of the simulated ELLJ is less than that of T18's. The restart of surface convection appears to be the death knell for the ELLJ in each instance. Apart from the ELLJ itself, there are other notable features that match in each graph, these being the existence of

NLLJ remnants prior to the onset of the mature PBL, and elevated average horizontal wind speeds after the collapse of the ELLJ. The NLLJ remnants are at once higher than simulated and of greater magnitude than that which was simulated, but in comparing the NLLJ of the first night of simulation to the second night with the second night's NLLJ being stronger, this makes sense. However, the simulated ELLJ's aftereffects on horizontal wind motion appear to be similar in magnitude to the observed elevated winds, possibly confirming a weakening in overall convective processes after the resolution of an eclipse.

4.f **Results Summary**

During the simulation which simulated the effects of a solar eclipse, the WRF YSU model was successfully able to replicate that the eclipse generated a temporary ELLJ as had been previously observed in T18. Persisting for no greater than two hours, wind speeds were found to be elevated much more aloft than at or near the surface.

The height of the PBL, ELLJ, and NLLJ are all located at elevations much lower than what one would expect based on physical evidence from T18 and theory as established in Markowski (2010). This may be due to improper PBL height buildup by the model, as the models were only provided with a single piece of initialization data and may have not had enough time to spin up prior to the time of interest. However, the temporal elements for which the ELLJ and NLLJ exist are consistent with what are predicted by T18 and Markowski (2010), respectively.

The results suggest that ELLJs are locally-forced, surface-induced, non-surface phenomena. The small spatial resolution effectively eliminates potential synoptic and mesoscale weather process influence, which take place over areas much larger than the simulated 12km x 12km grid. Additionally, topographically-forced ELLJ and NLLJ enhancement, as is common in the Great Plains, can also be eliminated from consideration due to this process occurring on a scale much larger than the model's resolution. The process is also too short-lived for Coriolis force to fully affect the ELLJ and bring it to a comparable NLLJ maximum.

However, a common mechanism must also be in place for NLLJ development, as some of these same processes that do explain general NLLJ occurrence are not in play within the environment of SCM. Instead, SCM-derived LLJ development seems entirely linked to the collapse of surface convective processes driven by insolation, which is validated by Fig. 3 from T18. The most likely remaining explanation for the depth and relative strength of the simulated ELLJ and NLLJ would be directly related to the frictional mixed layer force imbalance as predicted by Markowski (2010), Blackadar (1957), and Moene at al. (2010).

5. **Future Work**

In considering future in situ ELLJ research, new approaches are advised to study their effects. Observations within the lowest 50m of the surface should be considered too low to adequately capture ELLJ phenomena, which significantly reduces possible options for study. The

short response time for effects to manifest and dematerialize also renders standard radiosonde launches, even if launched at a 5-minute cadence, inaccurate for the time scale resolution necessary to capture the changes in dynamics aloft. Recommended methods for studying ELLJs tentatively include LiDAR instruments capable of penetrating the entrainment zone, airborne 'standard' instruments (e.g. thermometer, barometer, etc.) situated at a height of least 250m AGL by tethered balloons, and LiDAR instruments pointed both upwards and downwards from an aircraft moving at approximately 1000m AGL are all currently adequate options for proper monitoring of ELLJs.

Additional research on this subject would be to assess the minimum obscuration and highest latitudes for which ELLJs can occur in addition to which environments provide greatest promotion of ELLJ formation. Furthermore, assessing the strength of latent heat impacts on modeled ELLJ formation and studying the effects of 2-D and 3-D models on ELLJ formation and analyzing differences in structure would significantly enhance knowledge of ELLJ formation. Finally, manipulating Besselian elements to create custom eclipse events and analyzing hypothetical eclipse events would allow for the development of specific and transferrable eclipse events to experiment with effects on a variety of weather patterns.

References

Atmospheric and Environmental Research, Inc. (AER, Inc.). (2002). - *RRTM/RRTMG*. Rtweb.aer.com. http://rtweb.aer.com/rrtm_frame.html

Blackadar, A. (1957). Boundary Layer Wind Maxima and Their Significance for the Growth of Nocturnal Inversions. *Bulletin of the American Meteorological Society*, *38*(5), 283–290. https://doi.org/10.1175/1520-0477-38.5.283

Carruthers DJ. Stull R. B. 1988. An Introduction to Boundary Layer Meteorology, xiii + 666 pp. Dordrecht, Boston, London: Kluwer Academic Publishers. Price Dfl. 220.00, US $99.00, UK £64.00 (hardback). ISBN 90 277 2768 6; 90 277 2769 4 (paperback). *Geological Magazine*. 1989;126(3):308-309. doi:10.1017/S0016756800022433

Holton, J. R. (1967). The diurnal boundary layer wind oscillation above sloping terrain. *Tellus*, *19*(2), 200–205. https://doi.org/10.3402/tellusa.v19i2.9766

Hong, S.-Y., Noh, Y., & Jimy Dudhia. (2006). A New Vertical Diffusion Package with an Explicit Treatment of Entrainment Processes. *Monthly Weather Review*, *134*(9), 2318–2341. https://doi.org/10.1175/mwr3199.1

Hu, X.-M., Klein, P. M., & Xue, M. (2013). Evaluation of the updated YSU planetary boundary layer scheme within WRF for wind resource and air quality assessments. *Journal of Geophysical Research: Atmospheres*, *118*(18), 10, 490–410, 505. https://doi.org/10.1002/jgrd.50823

Jiménez, P. A., Dudhia, J., González-Rouco, J. F., Navarro, J., Montávez, J. P., & García-Bustamante, E. (2012). A Revised Scheme for the WRF Surface Layer Formulation. *Monthly Weather Review*, *140*(3), 898–918. https://doi.org/10.1175/mwr-d-11-00056.1

Jimy Dudhia. (1989). Numerical Study of Convection Observed during the Winter Monsoon Experiment Using a Mesoscale Two-Dimensional Model. *Journal of the Atmospheric Sciences*, *46*(20), 3077–3107. https://doi.org/10.1175/1520-0469(1989)046%3C3077:NSOCOD%3E2.0.CO;2

Lin, Y., R. D. Farley, and H. D. Orville, 1983: Bulk Parameterization of the Snow Field in a Cloud Model. *J. Appl. Meteor. Climatol.*, 22, 1065–1092, https://doi.org/10.1175/1520-0450(1983)022<1065:BPOTSF>2.0.CO;2.

Markowski, P., & Richardson, Y. (2011). *Mesoscale Meteorology in Midlatitudes*. John Wiley & Sons.

NASA. (2017). *Total Solar Eclipse 2017 Path USA Map*. https://eclipse2017.nasa.gov/static/img/eclipse-maps/nasa_eclipse_map_full.jpg

Torrecillas, M., Codina, B., & Zack, J. (2015). Implementation of the Bessel's method for solar eclipses prediction within the WRFARW model. In *Atmospheric Chemistry and Physics Discussions*. https://doi.org/10.5194/acp2015781

Turner, D. D., V. Wulfmeyer, Behrendt, A., Bonin, T. A., A. Choukulkar, Newsom, R. K., Brewer, W. A., & Cook, D. R. (2018). Response of the Land-Atmosphere System Over North-Central Oklahoma During the 2017 Eclipse. *Geophysical Research Letters*, *45*(3), 1668–1675. https://doi.org/10.1002/2017gl076908

Unidata Science Gateway. (2024). Ucar.edu. https://science-gateway.unidata.ucar.edu/. doi:10.5065/688s-2w73.

van, AF Arnold Moene, GJ Steeneveld, Baas, P., FC Bosveld, & Aam Holtslag. (2010). A Conceptual View on Inertial Oscillations and Nocturnal Low-Level Jets. *Journal of the Atmospheric Sciences*, *67*(8), 2679–2689. https://doi.org/10.1175/2010jas3289.1